3D Printing of Stainless Steel 316L for Corrosive and Low-pressure Environments

by

Venkata Krishnan Sampath

A Thesis Presented in Partial Fulfillment
of the Requirements for the Degree
Master of Science

Approved April 2021 by the
Graduate Supervisory Committee:

Bruno Azeredo, Chair
Cesar Torres
Bin Mu

ARIZONA STATE UNIVERSITY

May 2021

ABSTRACT

Corrosion is one of the key failure modes for stainless steel (SS) piping assets handling water resources managed by utility companies. During downtime, the costs start to incur as the field engineer procures its replacement parts. The parts may or may not be in stock depending on how old, complex, and common the part model is. As a result, water utility companies and its resilience to operate amid part failure are a strong function of the supply chain for replacement piping.

Metal additive manufacturing (AM) has been widely recognized for its ability to (a) deliver small production scales, (b) address complex part geometries, (c) offer large elemental metal and alloy selections, (d) provide superior material properties. The key motive is to harvest the short lead time of metal AM to explore its use for replacement parts for legacy piping assets in utility-scale water management facilities. In this paper, the goal was to demonstrate 3D printing of stainless-steel (SS) 316L parts using selective laser melting (SLM) technology. The corrosion resistance of 3D printed SS 316L was investigated using (a) Chronoamperometry (b) Cyclic Potentiodynamic Polarization (CPP) and Electrochemical Impedance spectroscopy (EIS) and its improved resistance from wrought (conventional) part was also studied. Then the weldability of 3D printed SS 316L to wrought SS 316L was illustrated and finally the mechanical strength of the weld and the effect of corrosion on weld strength was investigated using uniaxial tensile testing.

The results show that 3D printed part compared to the wrought part has a) lower mass loss before and after corrosion, (b) higher pitting potential and (c) higher charge transfer resistance. The tensile testing of welded dog bone specimens indicates that the 3D

printed parts despite being less ductile were observed to have higher weld strength compared to the wrought part. On this basis, metal AM holds great value to be explored further for replacement piping parts owing to their better corrosion resistance and mechanical performance.

TABLE OF CONTENTS

LIST OF TABLES

LIST OF FIGURES

CHAPTER 1 INTRODUCTION

Equipment failures under water, temperature, humidity and especially salt, among other environmental factors, cause metal structure and equipment to corrode and erode over time, wearing down components and leading things to function improperly or break down all together [1]. Erosion is wearing down of metal surface and coating occurs in an acidic or alkaline aggressive chemical environment along with high fluid surface velocity. Process water containing salts and ions such as Cl^- react with surfaces causing uniform and pitting corrosion leading to frequent failures of equipment that encounter water contact. The deterioration is the dissolution of iron from the metal into the environment, that could reduce strength of the structures.

Water utility companies are one of the strongly affected industry, requires an extensive corrosion protection as they are constantly exposed to water. In water utility companies, different atmospheric conditions come with different challenges, fresh water, or salty water. One of the problems in a freshwater environment is osmosis and cleaner the water the larger the risk of blisters and coating failure. Salty water contains dissolved salts and free ions such as Cl^- that attack the metal surface where there is potential difference. In water utility companies, the types of structures and equipment affected by the corrosion are pipelines & its parts such as fittings, pumps, pipe connectors. In the case of thermal power plants, massive structures such as water wheels, turbines, generators, accessory electric equipment, and miscellaneous power plant equipment are prone to corrosion caused failures.

The effect of corrosion on each of the major categories of structures and parts for thermal power plants is immense and the cost associated for protecting the structures is high. The amount of cost incurred for protecting the corrosion is around 20% [2]. The corrosion and replacement for corroded parts contribute to O&M cost which could increase the Levelized Cost of Energy (LCOE) for the thermal power. It is to be mentioned that the delay in fabrication of replacement conventional parts also contribute to the O&M cost and the supply chain management associated with getting the fabricated part from the external manufacturer.

The first Rapid prototyping was developed in 1980 to produce 3D prototype using computer aided design (CAD) [3]. The generation of rapid prototyping layer by layer known as Additive Manufacturing (AM). This paper focuses on focuses on Metal AM that has been widely recognized for its ability to (a) deliver small production scales (<100 units per year), (b) address complex part geometries, (c) offer a large elemental metal and alloy selections, and (d) achieve reasonable part density (i.e. >98%) and mechanical performance in both uniaxial, biaxial and torsion testing and its corresponding cyclic testing [4]. Although metal AM throughput is considerably slow (~1ft3/day, assuming a part that is 20% solid), if you consider the entire supply chain and its lead time, it creates opportunity and added value by having relatively fast turnaround time for production. This advantage has proven to be very resourceful and cost-effective in the aerospace industry to address uncertainties with suppliers of parts for aircrafts [2]. This paper aims to demonstrate mechanical, weldability and corrosion-resistance performance of 3D printed stainless steel piping.

This paper focuses on one the metal AM processes of Metals i.e., Powder Bed Fusion (PBF) via Selective Laser Melting (SLM). PBF is a subset of AM where high intensity power source such as Laser is used to melt/sinter powder layer by layer. It is further classified as: 1) SLM that uses high intensity laser source, 2) Electron beam melting (EBM) that uses electron beam source. The usage of SLM has become common due to its high resolution and accuracy. The SLM can produce highly dense parts (>99%) by changing laser scanning parameters [5]. SLM reduces the number of steps required in post-processing. Composition and microstructure can be significantly control using different printing material and utilizing number of printing parameters, and design of geometrical complex parts using CAD systems is achievable [6].

In SLM, A laser beam strikes the metal powder and forms a melt pool that led fast cooling rates (103 to 108 K/s). Moreover, the complex heat effect can be seen on a material, resulting in a different heat transfer processes when compared to casting and forging. Fast cooling results in a non-equilibrium solidification mechanism improves the limitation of solid solubility, grain refinement, and formation of metastable phases. Refined cellular and complex dendritic structures with a grain size of less than 1 μm can be seen between the laser tracks. The finer grain microstructure size leads to enhanced mechanical properties [7]. This rapid cooling and heating forms residual stress that can led to failure of 3D printed parts. The major disadvantage of SLM that it led to formation of residual stress due to rapid heating and cooling while printing. The residual stress present in the printed parts can be controlled by stress relief annealing heat treatment. It can be achieved via lower and higher temperature range. The lower temperature used to relieve the residual stress and higher temperature to improve microstructure resulting in recrystallized equiaxed grains [8].

SLM process produces a non-conventional sub granular structure resulting in grain refinement that significantly alter the surface and the bulk properties like the mechanical integrity, ductility, and machinability [9]. Weldability of the SLM printed 316L is also stated to be equal to the conventional SS 316L making it suitable to use additive manufacturing for replacement parts in place of SS 316L. The mechanical properties of the realized parts are acceptable, being dependent on the composition and the size of the metallic powder grains, and on the internal structure of the parts, process parameters, and the manufacturing strategy used.

Additive manufacturing is widely used in different domains of the industry, such as aerospace, automotive, consumer goods and medical field. The aerospace and defense industry are one of the earliest adopters of 3D printing, with the first use of the technology going back to 1989. Now, three decades later, A&D represents a 16.8% share of the $10.4 billion additive manufacturing market and heavily contributes to ongoing research efforts within the industry. Additive manufacturing for aerospace is not limited to prototypes, real functional parts are also being 3D printed and used in aircraft. A few examples of parts that can be produced with 3D printing include air ducts, wall panels and even structural metal components. Metal Additive manufacturing is increasingly being used in the manufacture of rockets. The technology is enabling engineers to innovate the design of rocket parts and manufacture them in a shorter time frame. One example of this is an injector head. Traditionally, injector heads are made from dozens or even hundreds of parts, which need to be machined and welded together. In contrast, 3D printing enables these components to be manufactured as a single piece, while casting and machining of injector heads used to take more than three months, the production time with AM was reduced to 35 hours with

a cost reduction up to 50%. The automotive industry is also a growing user of additive manufacturing: in 2019 alone, global automotive AM revenues reached $1.4 billion. Similarly, the industrial good sector is also adopting to additive manufacturing for its operational agility and shorter lead times [10]. From the State of Industry report (2018), 52% of those within the industrial goods sector favor AM most for its ability to reduce lead times. Since 3D printing requires no tooling, manufacturers can reduce the time needed to produce parts, bypassing a time-consuming and costly tooling production step.

In this study, the technical feasibility of using SLM printed stainless steel parts for pipeline systems was demonstrated through its corrosion resistance performance using chronoamperometry, cyclic potentiodynamic polarization (CPP), electrochemical impedance spectroscopy and microscopic characterization. Then the weldability of 3D printed SS 316L to wrought SS 316L and its mechanical strength is studied using uniaxial tensile testing. The long-term goal is to demonstrate that metal AM can significantly reduce downtime and costs associated with critical part replacements and increase resilience to uncertainty in the supply chain. We foresee a future in which utility companies will get a share of their replacement parts from a distributed network of metal AM providers rather than from the traditional metallurgy suppliers.

CHAPTER 2 3D PRINTING OF SS 316L

The Concept Laser M1, a commercial laser powder bed fusion (LPBF) metal additive manufacturing machine is used to 3d print the specimens. The printing parameters used are (a) a maximum laser power level of 100 Watts, (b) a laser scanning speed of Y mm/s, (c) a spot size of 0.05 mm, build plate dimensions of 90 x 90 mm^2. Stainless steel powders (i.e. SS316L) obtained from Praxair Inc.[11] was used to manufacture all 3d-printed specimens in this study. Argon was used as a shielding gas that was flown in the
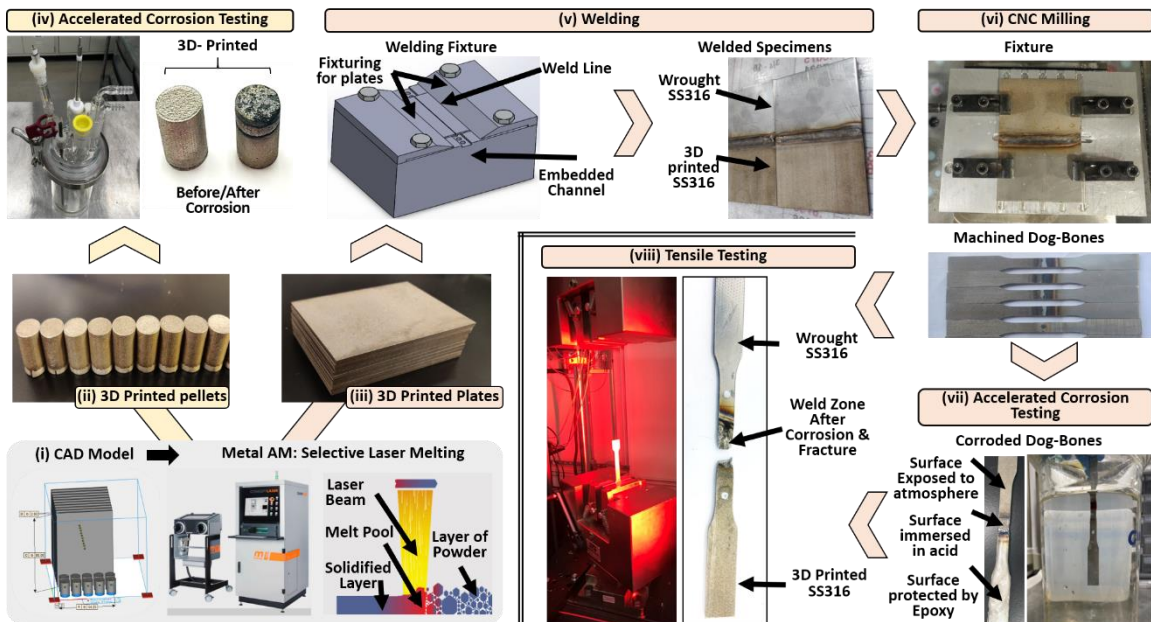
Figure 1 Flow diagram of the project from (i)3D printing of SS 316L to (viii) tensile testing of welded dogbones

direction of x-axis of build plate as shown in Supplementary Figure 1. During printing, the ventilator speed (which controls the flow of inert gas over the powder bed and carries ejected slag and smoke away from the laser spot) was set to 10% of its maximum rated capacity. The dosage of the powder (which refers to the amount of powder from the dose chamber added per each printed layer) was set to 300%. Ten plates (with dimensions: 54.25 mm x 80 mm x 2 mm) were printed 4 mm apart from each other as shown in Supplementary Figure 1 for making specimens for welding, corrosion, and mechanical testing and 32

6

cylindrical pellets (with dimensions: 9.2 mm in outer diameter and 12.7 mm in height) for corrosion testing.

Specimen Fabrication and Preparation

Conventional stainless steel 316L rods of outer diameter 9.2 mm were procured from McMaster Carr Inc. and used as a reference for comparison with the SLM 3D printed parts. Several conventional SS rods were cut to a length of 12.7 mm using a lathe. Additively manufactured SS 316L were printed as described previously. After fabrication, the top surface (i.e., surface to be exposed to etching solution) from both conventional and AM samples were grinded with SiC paper from grit size 140 to 600 to standardize their surface finish. The back of each samples (which is never exposed to the etching solution) was machined with a tapped hole for attachment to the sample holder of the electrochemical cell. Before the experiments, the samples were degreased with acetone, Iso propyl alcohol and finally washed with Deionized water.

CHAPTER 3 CORROSION PROPERTIES OF SS 316L

Experiment

Electrochemical Characterization Tests

Sodium Chloride 99% ACS grade and deionized water were used as the electrolyte in 2 M concentration for chronoamperometry test, and 0.64 M concentration for cyclic polarization and impedance spectroscopy. The number of specimens assigned to each of these tests is described in Table 1. A commercial etch cell (model: GAMRY 1L Multiport EC cell) with a total volume of 1L with a lid with ports for the working, counter and reference electrodes. The counter electrode was a graphite rod of 8 mm diameter and the reference electrode was Ag/AgCl in 3.5M KCl was used for conducting the electrochemical tests [12]. The voltage source was provided from Biologic AC 300 Potentiostat and the output variables were monitored using its commercial EC lab software.

Table 1: Specimens overview for comparison of 3D printed SS 316L and Wrought SS 316L

Material vs. Test Type	Conventional SS316L	3D Printed SS316L
Chronoamperometry	8	8
CPP/EIS	16	16

Chronoamperometry

For the chronoamperometry tests, all samples were weighted on a microbalance before and after this test to calculate its percentage mass loss. The SS 316L samples were immersed 1.1 mm into the etch solution for a total surface area of 1.27 cm^2 (calculated as the area of the top and sidewall surface of the immersed specimen). The samples are immersed for 30 min with the electrodes disconnected to stabilize and then, its open circuit

potential was measured. During the test, a constant potential of 1250 mV$_{Ag/AgCl}$ (Potential applied against Ag/AgCl and same notation used across the paper) was applied for 30 minutes and the corresponding current versus time plots were recorded in EC lab software. For the analysis of the results, the integral under the curve was calculated as a measure of the corrosion susceptibility of the stainless steel 316L.

Cyclic Potentiodynamic Polarization (CPP)

For the CPP and EIS tests, the solution was purged with argon gas for 30 minutes before immersing the sample. The open circuit potential (OCP) of the cell is measured after immersing the sample for 50 minutes or until the change in potential is negligible (i.e., less than 0.1 mV/s). The scan is started at the open circuit potential and moved in the positive direction at a scan rate of 0.5 mV/s with the current being recorded by the Potentiostat. The linear voltage increase was reversed when a current level of 5 mA was achieved, and it was allowed to return to the OCP value [13].

Electrochemical Impedance Spectroscopy

To estimate the surface resistance of the oxide film, the EIS analysis was carried out. The frequency sweep was set to span from 10000 Hz to 0.1 Hz for a sinusoidal potential of 10 mV$_{Ag/AgCl}$ and the current was collected with a frequency resolution of 8-10 points per Hertz to construct the Nyquist Plot [14].

Results & Discussion

Chronoamperometry

To study the corrosion susceptibility of 3D printed stainless steel (i.e., 316L), wrought and 3D printed cylindrical specimens were submitted to a constant
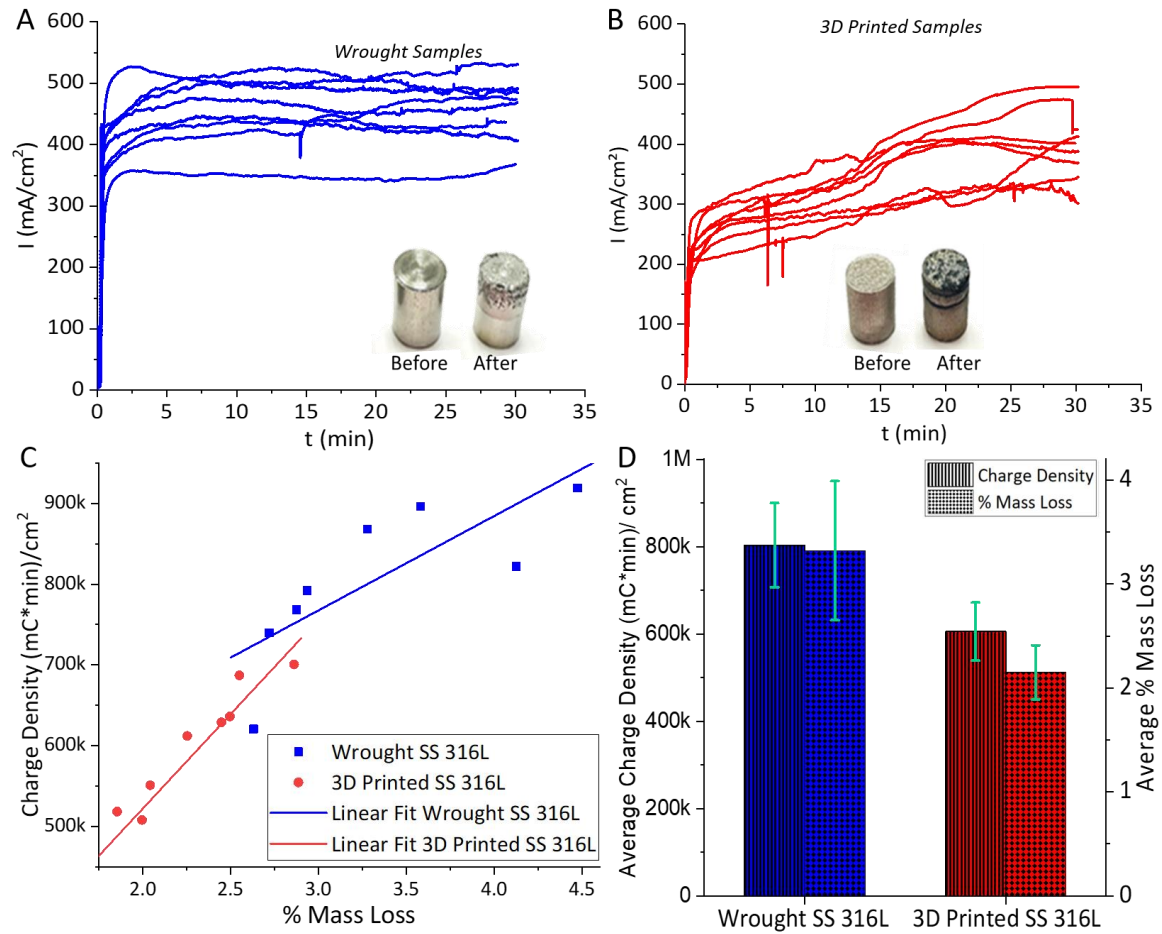
Figure 2 Chronoamperometry results for the wrought and 3D printed SS 316L samples A) Wrought SS 316L corrosion-time transient with the before and after corrosion inset B) 3D printed SS 316L corrosion-time transient with the before and after corrosion inset C) comparision of Integral under the curve- corrosion-time transient and % mass loss from gravimetric analysis

electrochemical potential (i.e., chronoamperometry) at room-temperature and the current density as a function of time was recorded (Figure 2 a-b) for up to 30 minutes. The magnitude of current density (j) is a measure of the ability of the oxide passivation layer to protect the underlying bulk grains and grain boundaries from corrosion. At a constant potential of 1250 $mV_{Ag/AgCl}$, the wrought SS 316L specimens exhibit an average steady-state current density of 464 mA/cm^2 with an incubation time (i.e., t_i, time period to achieve 95% of the steady state current) of 7.56 minutes whereas, in the case of the 3D printed SS 316L specimens, the average steady-state current density is 12% lesser and the incubation

10

time is 235% higher. These results suggest that the protection offered by the oxide film on the 3D printed SS 316L is higher than the wrought SS 316L possibly due to the reduction in its thickness followed by corrosion pitting by Cl$^-$ ions.

Those results were correlated to gravimetric analysis by calculating the percentage mass loss of the samples before and after the chronoamperometry test as shown in Figure 2 d. It is observed that the average mass loss (measured from 8 samples) for the wrought SS 316L is 55% higher than the 3D printed SS 316L, and that the average charge density (i.e. the time integral of current density) is 803,340 mC·min/cm^2 for the wrought SS 316L which is 33% higher than the 3D printed SS 316L. Additionally, the mass loss data has a linear correlation to the charge density for every individual sample tested (see Figure 2 c) and the higher slope of the fitted curve for 3D-printed data highlights its higher corrosion resistance. From the above data both the current density and the % mass loss show that the extent of corrosion is lesser in the 3D printed SS 316L than the Wrought SS 316L.

Cyclic Potentiodynamic Polarization (CPP)

Cyclic Potentiodynamic Polarization (CPP) was conducted to compare the passivity regions of the wrought SS 316L and 3D printed SS 316L in corrosive environments such as the presence of Cl$^-$ ions. The resulting parameter is the pitting potential E_{pit} also called the breakdown potential of the stainless steel which is the potential at which the corrosion accelerates after the breakdown of the passivity and E_{rev}-E_{OCV} is the width of the passivity region for 3D printed SS 316L and wrought SS 316L. After a rest period of 50 minutes, the open circuit potential (OCP) of the sample was recorded.

Polarization (Against Ag/AgCl) towards the positive side was scanned till the current of 5 mA is reached, and the potential is reversed to OCV of the sample.
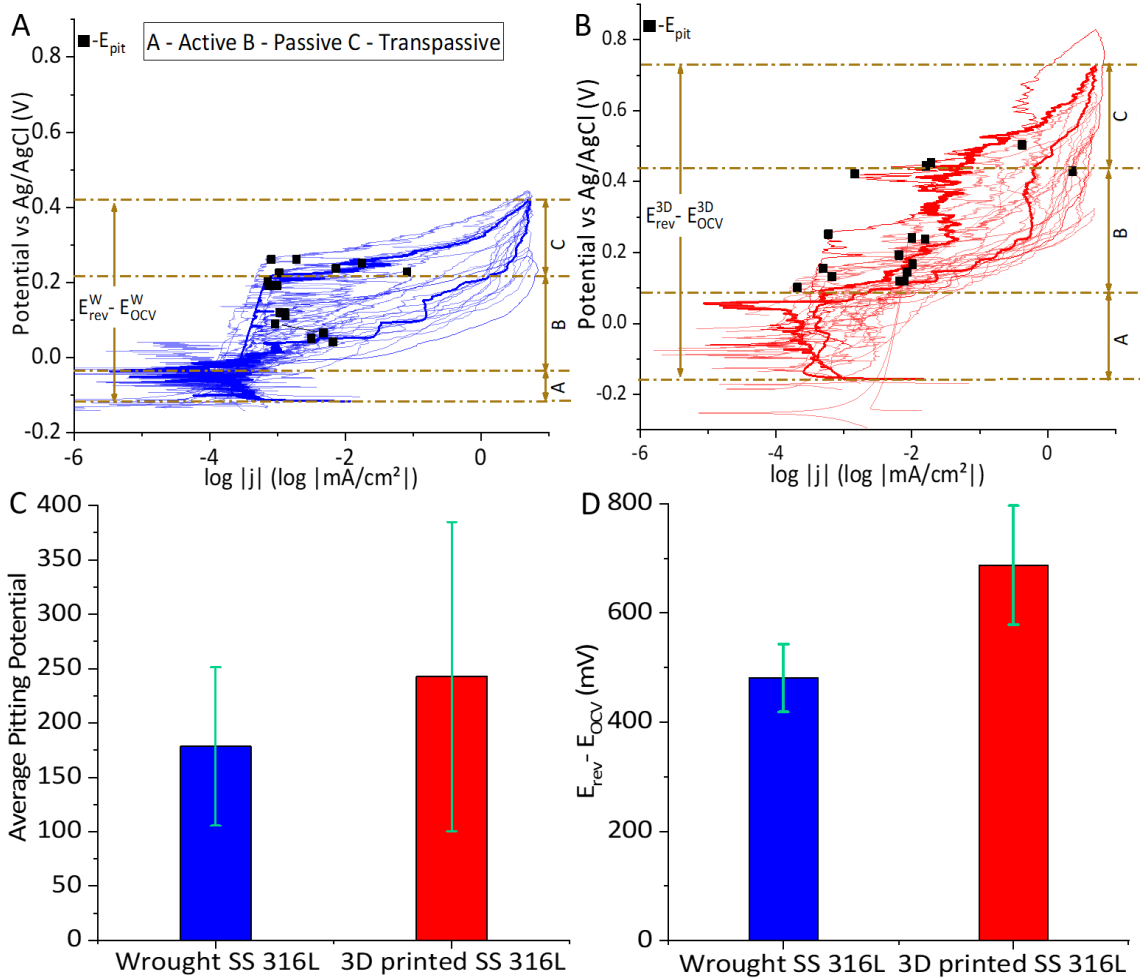
Figure 3 CPP test for the wrought and 3D printed SS 316L samples microstructure showing (a) the potential vs current plot for wrought SS 316L (b) the potential vs current plot for 3D printed SS 316L (note that the bold line denotes the sample with the mean pitting potential for each sample type) (b) the average pitting potential of all samples by sample type and (d) E_{rev}-E_{OCV} of all samples by samples type

The results were plotted between the Potential (against Ag/Agcl) and the logarithmic j, where j is the current recorded per unit area Figure 3 a and b. The pitting potential Epit is calculated as the inflection point where there is rapid increase in the current density for a small change in the potential and also the start of trans passivity of SS 316L as represented in Figure 3 a The average pitting potential of the Wrought SS 316L and 3D

12

printed SS 316L samples were calculated from 16 samples and plotted as a column chart

shown in Figure 3 c and the results show that the average pitting potential of 3D printed

SS 316L was 225 +/-95 Ag/Agcl mV and the wrought SS 316L was 171 +/- 75Ag/AgCl

mV because of the better stability of passive films in 3D printed 316L in corrosive

environments. In Figure 3 d the passivity width E_{rev} - E_{OCV} is shown and it is seen that the

passivity width for 3D printed SS 316L was 687 +/-113Ag/AgCl mV, and 42 % higher

than the wrought SS 316L (482 +/- 65Ag/AgCl mV) This characteristic is attributed to the

absence of MnS inclusions or precipitates on the surface of the 3D printed SS 316L, that

usually acts as the initiation sites for pitting corrosion. (REF). During the SLM 3D printing

process, the rapid solidification (typically $\sim 10^7$ K/s) reduces the diffusion time for MnS to

reach the surface and dissolves the MnS or (Ca, Al) oxides into the microstructure.

Electrochemical Impedance Spectroscopy

EIS was conducted to study the surface properties and resistance mechanism of the

wrought and 3D printed SS 316L from frequencies varying from 10000 Hz to 100 Hz with

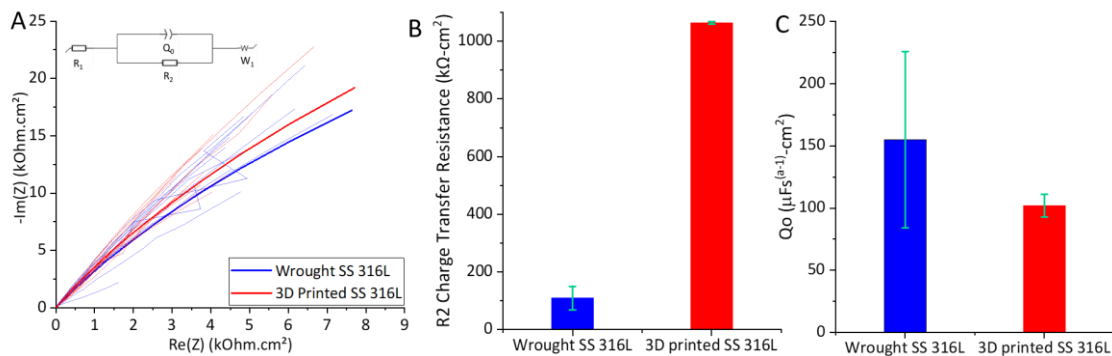a sinusoidal voltage of 10 m$V_{Ag/AgCl}$.

Figure 4 EIS test for the conventional and 3D printed SS 316L samples A) Nyquist Plot B) comparison of
charge transfer resistance C) Comparison of constant phase element Q_o

Nyquist plot (Figure 4 a) which is a complex plane plot of the impedance is used to find the different resistances across the surface layer of the samples. The lower frequencies of the sinusoidal voltage are associated with the charge transfer resistance R_2 and medium frequencies are associated with the double layer capacitance or constant phase element Q_o. In Figure 4 a, the larger diameter of the semicircle for 3D printed SS 316L shows the better stability of the oxide film and larger resistances. The Nyquist plot was fit with equivalent circuit that is a modified Randall's circuit to find the values of R_2 charger transfer resistance for the formation of corrosion species and Q_o constant phase element or double layer capacitance that represents the interfacial reactions on the electrode-electrolyte contact surface. The average values of charge transfer resistance and final phase element are plotted in Figure 4 b and c and it can be seen that the R_2 is higher in the 3D printed SS 316L confirming the improved barrier characteristics and Q_o which is associated with the double layer properties of the electrode-ions contact layer is lower in the 3D printed SS 316L. This shows that the defects on the oxide layer of 3D printed SS 316L is lesser than the wrought SS 316L. These results suggested that formation of a less defective and more compact oxide film on the surface of the 3D316L SS sample was associated to its fine sub–grain structure formed during the solidification process of selective laser melting [15]. The fine grain structure could significantly enhance the diffusion of cationic species towards oxide/electrolyte interface and to rapidly form the dense and least defective oxide film [16].

14

CHAPTER 4 PRESSURE TESTING OF SS 316L

To validate the use of additively manufactured pipes, testing against for industrial grade pressure is extremely important. First, a SS316L pressure vessel was designed, and 3D printed in our metal SLM machines and pressurized it to over 700 psi as a demonstration of the structural integrity of 3D printed pipes. The pipe was pressurized for 10 minutes before releasing the pressure. This was the maximum pressure it was tested against which is way higher than any pipe would have to endure in a commercial setting.
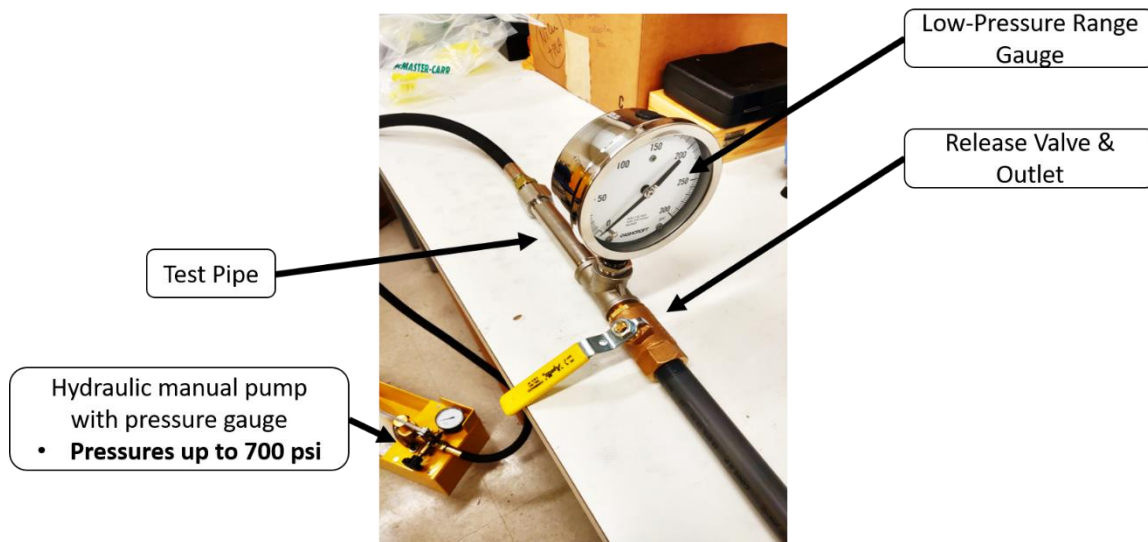
Figure 5 Pressure testing setup for 3D printed SS 316L

For continuous butt-welded (CBW) and electric resistance welded (ERW) pipe, the mill applied test pressure is ordinarily calculated from a constant mathematical formula known as the "Barlow Equation": $P = 2St/D$ where P = Test Pressure; S = Specified Yield Strength of Material; t = Wall thickness; D = Nominal outside diameter. The yield strength was safely assumed to be 550 MPa which is the average yield strength of SS 316L that is reported in literature. Two rules are also applied to the selection of test pressures: 1) Test pressures determined from the formula shall be rounded to the nearest 50 psi for pressures

below 1,000 psi and rounded off to the nearest 100 psi for pressures over 1,000 psi. 2)

Regardless of the value given by the formula, test pressure shall never exceed 2,500 psi for

outside diameters 3.500 inches or less, or 3,000 psi for outside diameters over 3.500 inches.

CHAPTER 5 WELDABILITY OF SS 316L

For application of 3D printed parts in the real world, it is critical that 3D-printed parts can be welded to wrought parts and form strong and corrosion resistant welds. In this task, a custom-build back-purged welding fixture will be used to weld dissimilar plates together using standard welding rods ER316L (i.e., Cr-Ni-Mo-Mn alloy).

Welding of Wrought and 3D printed SS316L Plates and Milling of Dog bones

A back purged welding fixture was designed as shown in Supplementary Figure 5 to weld the following new specimens wrought to wrought plates and wrought-to-3D-printed plates which are referred to by the following acronyms: W-W and W-3D Printed, respectively. The tungsten inert gas (TIG) welding process was used following AWS D1.6 Structural Welding Code - Stainless Steel with a filler metal rod of the following alloy AWS ER316L (Cr-Ni-Mo-Mn alloy) to weld the plates [17] .

Specimen design and CNC Milling of dog-bones from welded plates.

Finally, the welded plates must go through a milling operation to cut dog bones out of the welded plates. The tensile test specimen geometry was designed based on ASTM E8 standard. This standard provides various geometries of specimen broadly classified as plate type and round specimens (ASTM E8, 2010) [18]. Plate type specimen, as shown in Supplementary Figure 2, was selected for this study. A fillet radius of 18 mm was used, and the stress concentration factor is estimated to be 1.08 in literature [19] The final design of specimen is shown in Supplementary Figure 4 and, after milling, it has the following dimensions: (i) total length of 108.5 mm, (ii) gauge section length of 25 mm, (iii) gauge section width of 6 mm and (iv) gripper section width of 10 mm. All these lateral dimensions

of the dog bones were of same on either side of the welded zone since milling of the welded plates cuts identical dimensions. However, thickness variations in the 3D-printed and wrought sides exist mostly due to thickness errors in the 3D printed parts. The average thickness of the final specimens was (i) 1.924 mm on the wrought side with a standard deviation of 0.0340 mm, (ii) 2.066 mm on the 3d printed side with a standard deviation of 0.018 mm and, (iii) 2.254 mm on the weld zone with a standard deviation of 0.131 mm. The cutting fixture as shown in Supplementary Figure 3 is used to secure the plates and the parts are milled on a CNC machine.

CHAPTER 6 MECHANICAL PROPERTIES OF SS 316L

Experiment

A 250kN load capacity universal testing machine (model: Instron 5985) was used to perform tensile tests. All the tests were conducted at a strain rate of 10^{-3} s^{-1} following ASTM E8 standard. Prior to the tensile test, the specimen's cross-section thickness was measured using a vernier caliper at the 3D printed side, the wrought side and at the weld. A non-contact video extensometer was used for strain measurements. For the extensometer to recognize the deformation, two white spots were marked in the gauge section of the specimen. The extensometer was calibrated, and load cell and displacement were set to zero, each time a new specimen was loaded on the machine. Force and displacement data was acquired from the machine and the samples were brought to complete fracture. To compute the engineering stress, young's modulus, yield stress and ultimate stress, it was necessary to select the initial cross-section area. Given the small variations in thickness in the wrought, 3D printed and weld zone, the cross-section area selected corresponded to the location of the neck and failure zone (e.g., if the specimen necked and failed at the wrought side, its cross-section area was used to compute stress). The specimen types produced for mechanical testing and its sample size are described in Table 2.

Corrosion of Welded Dog Bones

To study the effect of corrosion on the mechanical properties of the weld zone between the 3D printed and wrought SS 316L, a set of welded dog bones were corroded using constant positive potential against Ag/AgCl electrode before conducting the tensile test. In preparation for this step, it was critical to limit the surface area to be corroded around the weld zone of the specimens to 1 cm^2 which is identical to the surface area of

the pellets immersed in solution and allows for a direct comparison with that dataset despite difference in geometry. The bottom of the welded dog bones was encapsulated with epoxy to protect it and the upper half of the dog bones was not immersed in the electrolyte and was connected to the circuit Figure 1 (vii). A constant potential of 1250 mV$_{Ag/AgCl}$ for 45 min was applied, after which the samples were dried, epoxy was scrapped off for the tensile test.

Table 2 Design of Experiments for corrosion and mechanical testing of welded dogbones

Sample Type	Number of Specimens	Corrosion Time, min	Potential mV
Wrought to Wrought	4	NA	NA
Wrought to 3D printed	12	NA	NA
Wrought to 3D printed (Corroded)	12	45	1250

Results & Discussion

Uniaxial tensile tests were performed on three sample types: non-corroded wrought-to-wrought (W-W non-corroded), non-corroded wrought-to-3D printed (W-3D non-corroded) and corroded printed (W-3D corroded). wrought-to-3D printed (W-3D corroded). From now onwards, the wrought-to-wrought non-corroded samples will be referred to as the "reference" samples. Stress versus strain curves are plotted for total of 24 specimens and color coded by sample type to compare their mechanical performance (See Figure 6). It is found that a few specimens broke at wrought side instead of weld zone. One of the parameters that explains this behavior is that 3D printed side was marginally thicker by 6.9 % when compared to the wrought side that leads to higher stress

20

concentration on the wrought side resulting in failure. In addition, the 3D printed parts were expected to exhibit high strength due to the presence of unique microstructure formed during SLM printing. According to literature, SLM 3D printed parts have 25% higher ultimate strength and 49% higher yield strength as compared to wrought/cast counterparts [3]. Combination of these two effects led to the failure of specimens at the wrought side.

Bar plots reported in Figure 7 shows the comparison of mechanical properties derived from uniaxial tensile test of all the specimens. Non-Corroded W-3D specimens have 8.47% less yield strength when compared to reference specimens. Given that none of the samples broke at the 3D printed side, it is possible to conclude that the interface
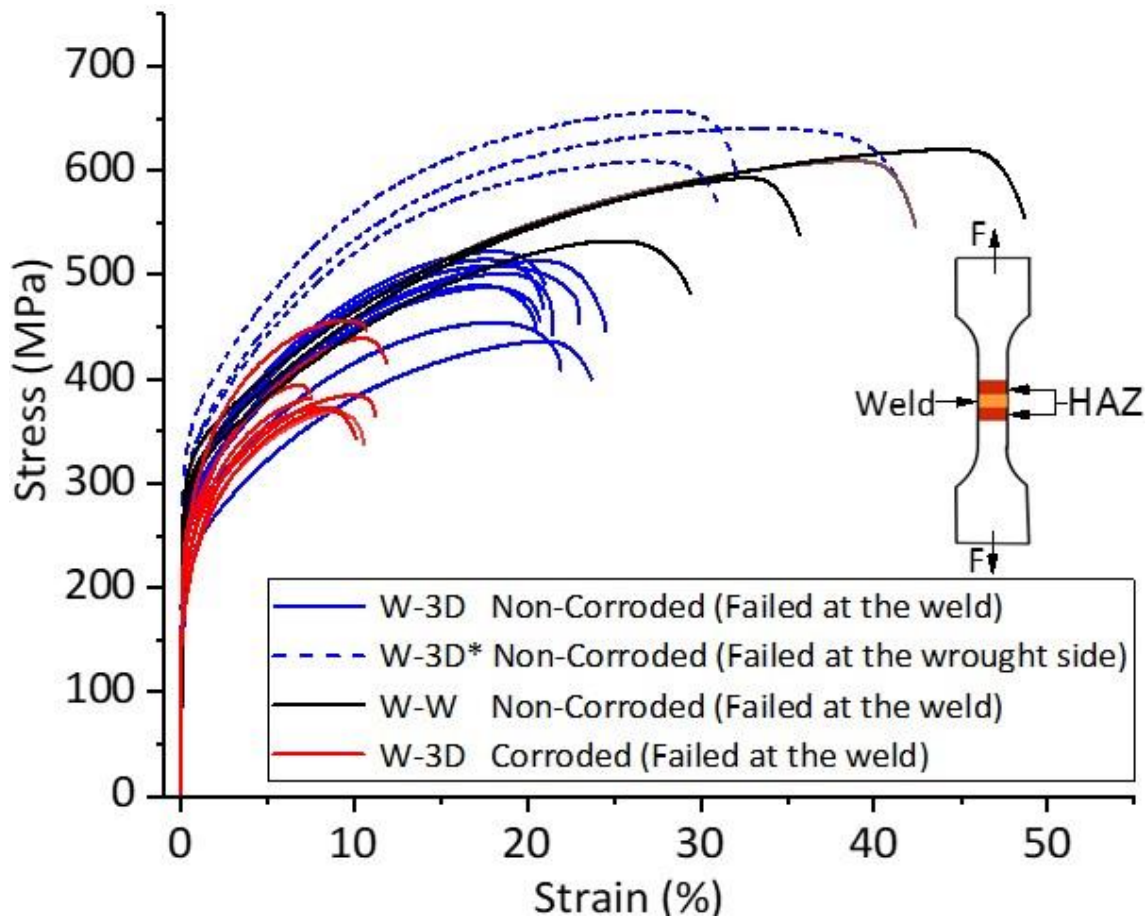

Figure 6 Mechanical Tensile Testing Stress (MPa) vs Strain (%) curve for W-W Non corroded, W-3D Non Corroded, W-3D corroded

21

between 3D printed parts and the weld zone is almost as strong as the weld interface with the wrought side. Not only the yield, but also the ultimate strength is 11.51% lower in the non-corroded W-3D specimens compared to the reference which is a small difference.
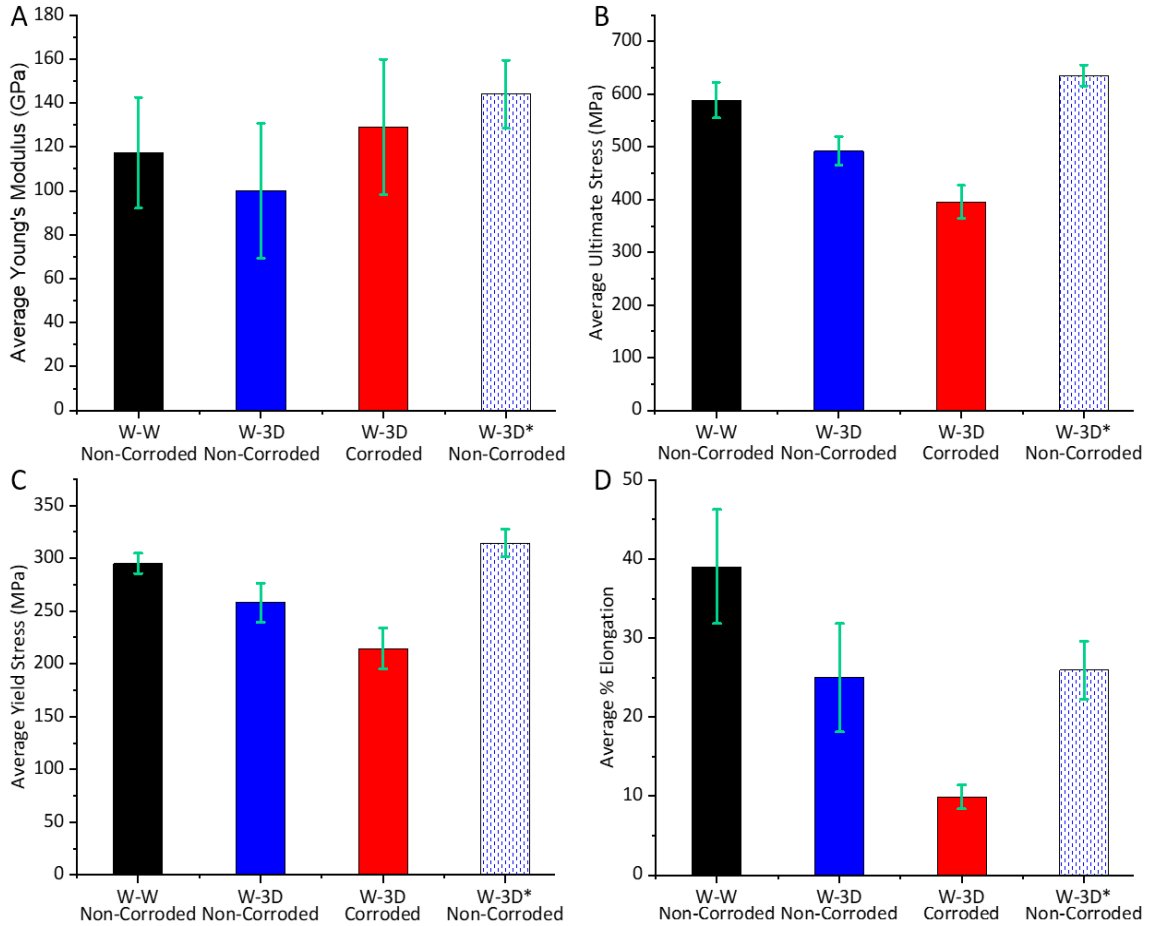
Figure 7 Comparison of mechanical properties by sample type derived from uniaxial tensile tests for W-W non-corroded, W-3D non-corroded, W-3D* non-corroded and W-3D corroded specimens, including: (a) average Young's modulus, (b) average ultimate stress, (c) average yield stress, and (d) average percentage elongation

However, the non-corroded W-3D specimens clearly exhibit a significantly lower ductility that is 54.79 % lower than reference specimens. This dramatic reduction in ductility is associated with the small grain size microstructure of the 3D printed part and its resulting microstructure at the weld zone. Specimens that broke at the wrought side

22

retained the ductility and those that broke at the weld exhibit lower ductility [3], [20] On the other hand, corrosion has considerably affected the mechanical properties of the specimens under uniaxial tensile test which is mainly caused by the penetration of corrosion agents such as Cl^- on to the surface and reducing the strength of the specimen. From the Figure 7 d corroded W-3D specimens has 154.86% less ductility when compared to the non-corroded W-3D specimens. The drastic reduction in ductility of the corroded specimens is due to occurrence of different mechanisms including the hydrogen embrittlement due to hydrogen evolution during the electrochemical reaction, alteration of chemical compositions due to corrosive agents, change in morphology of the steel, and the concentration of residual stress on the surface of the specimen [21]. The yield strength and the ultimate strength of the corroded W-3D specimens are 26.80% and 33.32% less than the non-corroded W-3D specimens as shown in Figure 7 b and c. This relatively less variation is because the corrosion affects only 0.1 mm deep from the surface and the moderate change in the yield strength and the ultimate strength caused by the reduction the thickness of the specimen, corrosion products formed due to the chemical reaction and increased surface roughness due to corrosion pit [22], [23]. These results show that the welding strength between dissimilar manufactured parts are as strong as conventional W-W welded specimens. It is seen that the ductility is the most affected mechanical property in W-3D non-corroded and W-3D corroded when compared to W-W non-corroded. This loss in ductility is associated with the porosity of the internal structure and thermal stresses which can be improved by tailoring the 3D printing parameters such as laser power, laser scanning speed and build orientation [24].

CHAPTER 7 MICROSTRUCTURE ANALYSIS OF SS 316L

Experiment

The cylindrical specimens submitted to chronoamperometry underwent microstructural analysis. Firstly, the morphology of the samples before and after corrosion was characterized using Scanning Electron Microscopy (SEM) images and Energy-dispersive X-ray spectroscopy (EDS) data at accelerating voltage of 15 kV (Phillips XL-30). SEM images and EDS data were taken from 5 different random locations from within a 1 mm radius from the center of the stainless-steel cylindrical specimens. Images were taken at the same brightness and contrast digital values set by the SEM software.

Results & Discussion

Figure 8 SEM Micrographs of A) Wrought SS 316L and B) 3D printed SS 316L after the same corrosion conditions

The SEM Micrographs of the wrought SS 316L and the 3D printed SS 316L were obtained after the same chronoamperometry test us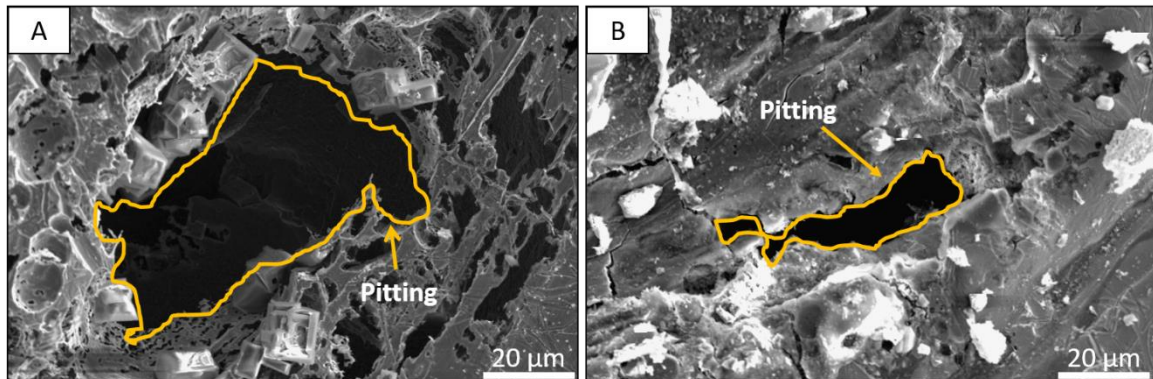ing SEM - FEG XL30 (FEI) at Eyring Materials Center, ASU. Figure 8 SEM Micrographs of A) Wrought SS 316L and B) 3D printed SS 316L after the same corrosion conditions shows the surface morphology of (a) wrought SS 316L and (b) 3D printed SS 316L. The Wrought SS 316L has strongly corroded and therefore the pit density and pit sizes were greater than the 3D printed SS

316L. This shows that the extent of corrosivity is higher in the wrought SS 316L and that are in good consent with the results of chronoamperometry, cyclic potentiodynamic polarization and electrochemical impedance spectroscopy. The corrosion products formed were also seen on the surface which can sometimes protect the further corrosion on the
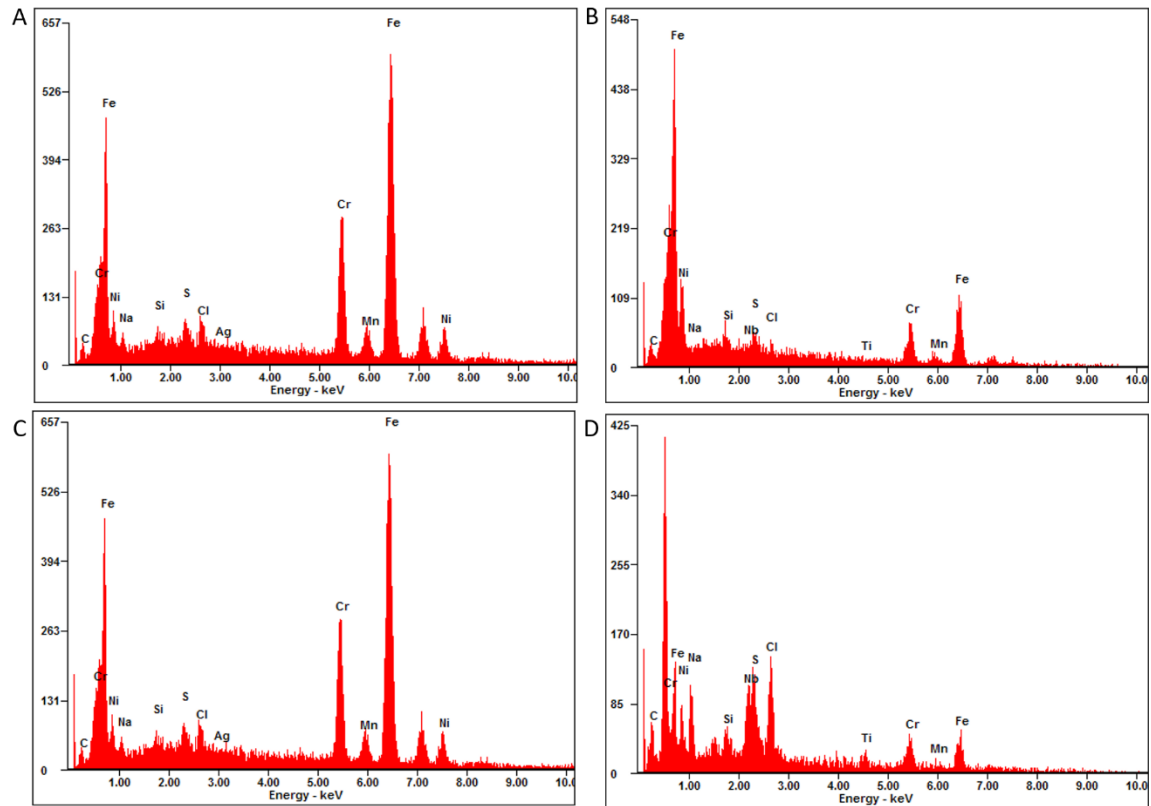
Figure 9 EDS analysis of (a) wrought SS 316L before corrosion (b) 3D printed SS 316L before corrosion (c) wrought SS 316L after corrosion (d) 3D printed SS 316L after corrosion

metal surface.

EDS elemental mapping of the surface after corrosion showed the percentage of Mn, Si, C, Cr and other elements of the SS 316L. Figure 9 shows that the MnS or other oxide precipitates are lesser on the 3D printed SS 316L by 46%, which is attributed to the high solidification rate seen in the selective laser melting whereas the wrought SS 316L shows a higher percentage of precipitates [25]. It is also observed that the C% on the MnS precipitate rich wrought SS 316L was also low compared to the 3D printed SS316L.

CHAPTER 8 CONCLUSION

The Stainless Steel (SS) 316L was additive manufactured using selective laser melting (SLM) 3D printing process in in different shape and size including cylindrical pellets, plates, and half dog bones. The corrosion properties of the 3D printed specimens were tested using the experiments 1) Chronoamperometry, 2) Cyclic Potentiodynamic Polarization (CPP) and 3) Electrochemical Impedance Spectroscopy (EIS) and compared with wrought SS 316L. The 3D printed half dog bones were welded to wrought dog bones and mechanical strength of the welded dog bones were studied using uniaxial tensile test to find the 1) young's modulus 2) ultimate stress 3) yield stress and 4) percentage elongation. The microscopic characterization was done using SEM and EDS analysis. The experimental work is summarized in Figure 9 and the following are the conclusions:

(i)   The corrosion susceptibility of the 3D printed SS 316L is lesser than wrought SS 316L as seen from the chronoamperometry results. The average percentage mass loss and average charge density of the wrought SS 316L were 55% and 33% higher than the 3D printed SS 316L.

(ii)   The resistance to pitting initiation is higher for 3D printed SS 316L with the pitting potential 42% higher than wrought SS 316L that is attributed to lesser precipitates on the surface from high solidification rate in selective laser melting.

(iii)   Electrochemical Impedance Spectroscopy (EIS) test revealed that charge transfer resistance of 3D printed SS 316L is higher than wrought 316L because of the lesser defects.

(iv)   The SEM imaging showed that the corrosion pit size is much wider for the wrought SS 316L than 3D printed SS 316l for the same corrosion conditions. EDS analysis showed the Mn percentage on the surface that forms MnS precipitates was less on the 3D printed SS 316L and are in good consent with the three electrochemical tests.

(v)   The tensile testing of the wrought to 3D printed dog bones established that the weld interface between 3D printed part and wrought part is almost as strong as the weld interface between two wrought parts. Also, ductility is the highly affected mechanical property in wrought to 3D non-corroded and wrought to 3D corroded specimens when compared to wrought to wrought non-corroded.
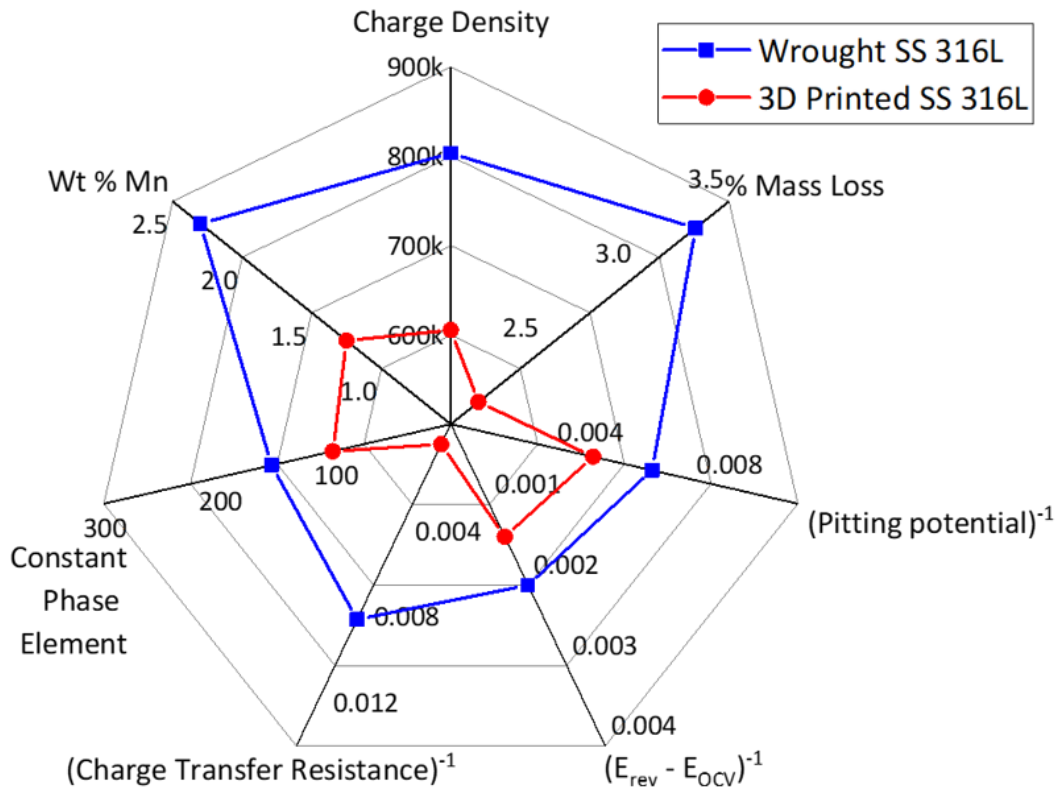

Figure 10 Radial plot comparing the corrosion resistance of wrought SS 316L and 3D printed SS 316L

REFERENCES

[1]   A. Moncmanová, "CHAPTER 1 Environmental factors that influence the deterioration of materials," vol. 28, pp. 1–25, doi: 10.2495/978-1-84564-032-3/01.

[2]   F. Report, "P i p e l i n e C o r r o s i o n," no. November, 2008.

[3]   Y. M. Wang *et al.*, "Additively manufactured hierarchical stainless steels with high strength and ductility," *Nat. Mater.*, vol. 17, no. 1, pp. 63–70, 2018, doi: 10.1038/NMAT5021.

[4]   A. Sharstniou, S. Niauzorau, P. M. Ferreira, and B. P. Azeredo, "Electrochemical nanoimprinting of silicon," *Proc. Natl. Acad. Sci. U. S. A.*, vol. 116, no. 21, pp. 10264–10269, 2019, doi: 10.1073/pnas.1820420116.

[5]   U. Prasad *et al.*, "Enhanced Photoelectrochemical Water Splitting with Er- and W-Codoped Bismuth Vanadate with WO3 Heterojunction-Based Two-Dimensional Photoelectrode," *ACS Appl. Mater. Interfaces*, vol. 11, no. 21, pp. 19029–19039, 2019, doi: 10.1021/acsami.9b00150.

[6]   D. Kong *et al.*, "Bio-functional and anti-corrosive 3D printing 316L stainless steel fabricated by selective laser melting," *Mater. Des.*, vol. 152, pp. 88–101, 2018, doi: 10.1016/j.matdes.2018.04.058.

[7]   B. Song *et al.*, "Differences in microstructure and properties between selective laser melting and traditional manufacturing for fabrication of metal parts: A review," *Front. Mech. Eng.*, vol. 10, no. 2, pp. 111–125, 2015, doi: 10.1007/s11465-015-0341-2.

[8]   R. Stress and C. Characteristics, "Additive Manufactured 316L Stainless-Steel Samples: Microstructure, Residual Stress and Corrosion Characteristics after Post-Processing," 2021.

[9]   N. Haghdadi, M. Laleh, M. Moyle, and S. Primig, "Additive manufacturing of steels : a review of achievements and challenges," *J. Mater. Sci.*, vol. 56, no. 1, pp. 64–107, 2021, doi: 10.1007/s10853-020-05109-0.

[10]   AMFG, "Industrial Applications of 3D Printing: The Ultimate Guide," 2021. amfg.ai/industrial-applications-of-3d-printing-the-ultimate-guide/.

[11]   U.A, "Safety Data Sheet," *Mater. Saf. Data Sheet*, vol. 4(2), no. 034034, pp. 8–10, 2012.

[12]   C. Material and P. Databases, "Making Potentiodynamic Anodic Polarization," pp. 1–8, 2013, doi: 10.1520/G0005-13.2.

[13]   ASTM International, "ASTM G61.19448 Standar Test Method for Conducting

Cyclic Potentiodynamic Polarization Measureements for Localized Corrosion Susceptibility of Iron-Nickel or Cobalt-Based Alloys," *ASTM Stand.*, vol. 86, no. Reapproved, pp. 1–5, 2018, doi: 10.1520/G0061-86R18.2.

[14] ASTM Norma G 106, "Standard Practice for Verification of Algorithm and Equipment for Electrochemical Impedance Measurements," *Astm*, vol. 03, no. Reapproved, pp. 1–11, 1999, doi: 10.1520/G0106-89R15.2.

[15] M. J. K. Lodhi, K. M. Deen, M. C. Greenlee-wacker, and W. Haider, "Additively manufactured 316L stainless steel with improved corrosion resistance and biological response for biomedical applications," *Addit. Manuf.*, vol. 27, no. January, pp. 8–19, 2019, doi: 10.1016/j.addma.2019.02.005.

[16] B. Zhang, Y. Li, and F. Wang, "Electrochemical corrosion behaviour of microcrystalline aluminium in acidic solutions," *Corros. Sci.*, vol. 49, no. 5, pp. 2071–2082, 2007, doi: 10.1016/j.corsci.2006.11.006.

[17] A. American and N. Standard, "Structural Welding Code- Stainless Steel," 1999.

[18] ASTM E8, "ASTM E8/E8M standard test methods for tension testing of metallic materials 1," *Annu. B. ASTM Stand. 4*, no. C, pp. 1–27, 2010, doi: 10.1520/E0008.

[19] D. A. Patil, "Effects of Increasing Layer Thickness in the Laser Powder Bed Fusion of Inconel 718," *Unpubl. Master's thesis*, no. Arizona State University, 2019.

[20] P. Rawn, "3D PRINTING OF 316L STAINLESS STEEL AND ITS EFFECT ON MICROSTRUCTURE AND MECHANICAL PROPERTIES by Penn Rawn A thesis submitted in partial fulfillment of the requirements for the degree of Masters of Science in Metallurgical Engineering and Mineral Process," pp. 1–88, 2017.

[21] L. Li, M. Mahmoodian, and C. Q. Li, "Effect of corrosion on mechanical properties of steel bridge elements," *Maintenance, Safety, Risk, Manag. Life-Cycle Perform. Bridg. - Proc. 9th Int. Conf. Bridg. Maintenance, Saf. Manag. IABMAS 2018*, no. July, pp. 1783–1790, 2018, doi: 10.1201/9781315189390-243.

[22] R. Winston Revie, "Corrosion and Corrosion Control: An Introduction to Corrosion Science and Engineering," *WILEY*, vol. ISBN: 978-, no. 4th, 2008.

[23] Y. Hou, D. Lei, S. Li, W. Yang, and C. Q. Li, "Experimental Investigation on Corrosion Effect on Mechanical Properties of Buried Metal Pipes," *Int. J. Corros.*, vol. 2016, 2016, doi: 10.1155/2016/5808372.

[24] Z. Sun, X. Tan, S. B. Tor, and C. K. Chua, "Simultaneously enhanced strength and ductility for 3D-printed stainless steel 316L by selective laser melting," *NPG Asia Mater.*, vol. 10, no. 4, pp. 127–136, 2018, doi: 10.1038/s41427-018-0018-5.

29

[25] Q. Chao *et al.*, "Scripta Materialia On the enhanced corrosion resistance of a selective laser melted austenitic stainless steel," *Scr. Mater.*, vol. 141, pp. 94–98, 2017, doi: 10.1016/j.scriptamat.2017.07.037.

[26] J. R. Trelewicz, G. P. Halada, O. K. Donaldson, and G. Manogharan, "Microstructure and Corrosion Resistance of Laser Additively Manufactured 316L Stainless Steel," vol. 68, no. 3, pp. 850–859, 2016, doi: 10.1007/s11837-016-1822-4.

[27] Y. Zhang *et al.*, "Corrosion mechanism of amorphous alloy strengthened stainless steel composite fabricated by selective laser melting," *Corros. Sci.*, no. March, p. 108241, 2019, doi: 10.1016/j.corsci.2019.108241.

[28] K. Saeidi, X. Gao, Y. Zhong, and Z. J. Shen, "Materials Science & Engineering A Hardened austenite steel with columnar sub-grain structure formed by laser melting," vol. 625, pp. 221–229, 2015, doi: 10.1016/j.msea.2014.12.018.

[29] R. F. Schaller, J. M. Taylor, and E. J. Schindelholz, "Corrosion Properties of Powder Bed Fusion Additively Manufactured 17-4 PH Stainless Steel."

[30] C. Örnek, "Additive manufacturing – a general corrosion perspective," vol. 2782, 2018, doi: 10.1080/1478422X.2018.1511327.

[31] P. K. Gokuldoss, S. Kolla, and J. Eckert, "Additive Manufacturing Processes : Selective Laser Melting , Electron Beam Melting and Binder," 2017, doi: 10.3390/ma10060672.

[32] J. D. Strickland and D. Ph, "Applications of Additive Manufacturing in the Marine Industry," no. September, 2016, doi: 10.13140/RG.2.2.29930.31685.

[33] J. R. Scully and N. Birbilis, "Corrosion of Additively Manufactured Alloys : A Review," vol. 9312, pp. 1318–1350, 2018.

[34] G. Sander, S. Thomas, V. Cruz, M. Jurg, N. Birbilis, and X. Gao, "On The Corrosion and Metastable Pitting Characteristics of 316L Stainless Steel Produced by Selective Laser Melting," vol. 164, no. 6, pp. 250–257, 2017, doi: 10.1149/2.0551706jes.

[35] M. J. K. Lodhi, K. M. Deen, and W. Haider, "Corrosion behavior of additively manufactured 316L stainless steel in acidic media," *Materialia*, vol. 000, no. June, pp. 1–11, 2018, doi: 10.1016/j.mtla.2018.06.015.

[36] D. Kong, X. Ni, C. Dong, and X. Lei, "PT," *Mater. Des.*, no. 2017, p. #pagerange#, 2018, doi: 10.1016/j.matdes.2018.04.058.

[37] D. Kong, C. Dong, X. Ni, and X. Li, "Corrosion of metallic materials fabricated by selective laser melting," no. November 2018, 2019, doi: 10.1038/s41529-019-

0086-1.

[38]   N. F. El Boraei and M. A. M. Ibrahim, "Comparative study on the corrosion behaviour of Lord Razor Blade Steel (LRBS) in aqueous environments in aqueous environments," vol. 3655, 2020, doi: 10.1080/16583655.2020.1742473.

[39]   G. Sander, J. Electrochem, and C. Soc, "On The Corrosion and Metastable Pitting Characteristics of 316L Stainless Steel Produced by Selective Laser Melting On The Corrosion and Metastable Pitting Characteristics of 316L Stainless Steel Produced by Selective Laser Melting," 2017, doi: 10.1149/2.0551706jes.

APPENDIX A

SUPPLEMENTARY FIGURES
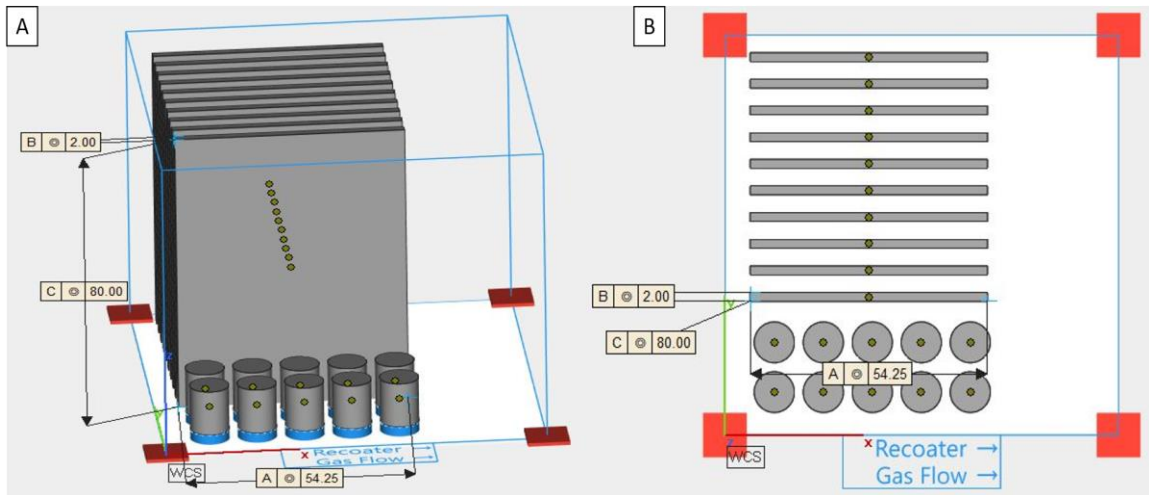
Supplementary Figure 1: A) Iso view of build plate design and B) Top view of build plate design

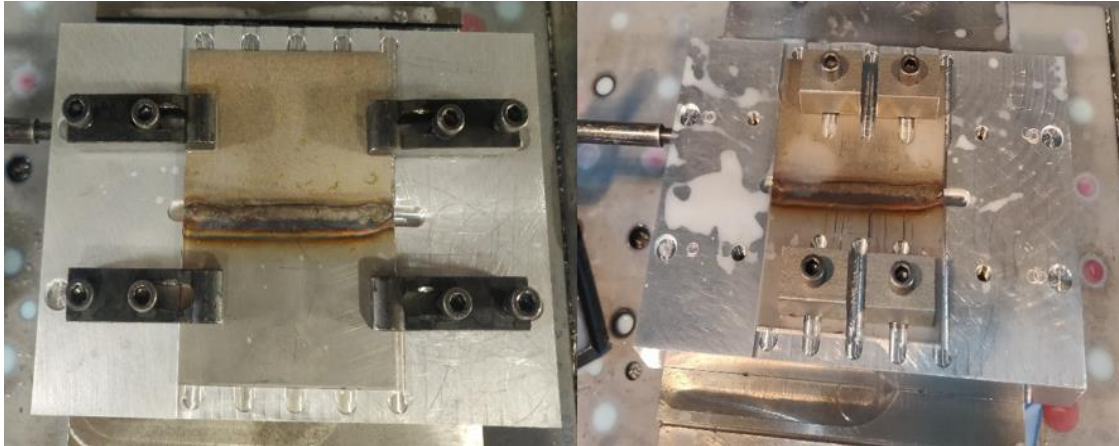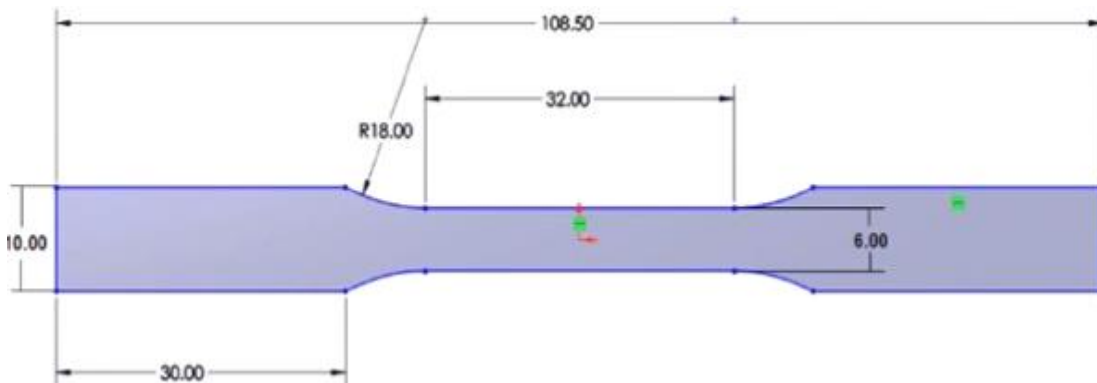| Dimensions			
	Standard Specimens		Subsize Specimen
	Plate-Type, 40 mm [1.500 in.] Wide	Sheet-Type, 12.5 mm [0.500 in.] Wide	6 mm [0.250 in.] Wide
	mm [in.]	mm [in.]	mm [in.]
G—Gage length (Note 1 and Note 2)	200.0 ± 0.2 [8.00 ± 0.01]	50.0 ± 0.1 [2.000 ± 0.005]	25.0 ± 0.1 [1.000 ± 0.003]
W—Width (Note 3 and Note 4)	40.0 ± 2.0 [1.500 ± 0.125, -0.250]	12.5 ± 0.2 [0.500 ± 0.010] thickness of material	6.0 ± 0.1 [0.250 ± 0.005]
T—Thickness (Note 5)			
R—Radius of fillet, min (Note 6)	25 [1]	12.5 [0.500]	6 [0.250]
L—Overall length, (Note 2, Note 7, and Note 8)	450 [18]	200 [8]	100 [4]
A—Length of reduced section, min	225 [9]	57 [2.25]	32 [1.25]
B—Length of grip section (Note 8)	75 [3]	50 [2]	30 [1.25]
C—Width of grip section, approximate (Note 4 and Note 9)	50 [2]	20 [0.750]	10 [0.375]

Supplementary Figure 2: ASTM E8 Standards for plate geometry

Supplementary Figure 3: Cutting fixture assembly with welded plate fixed
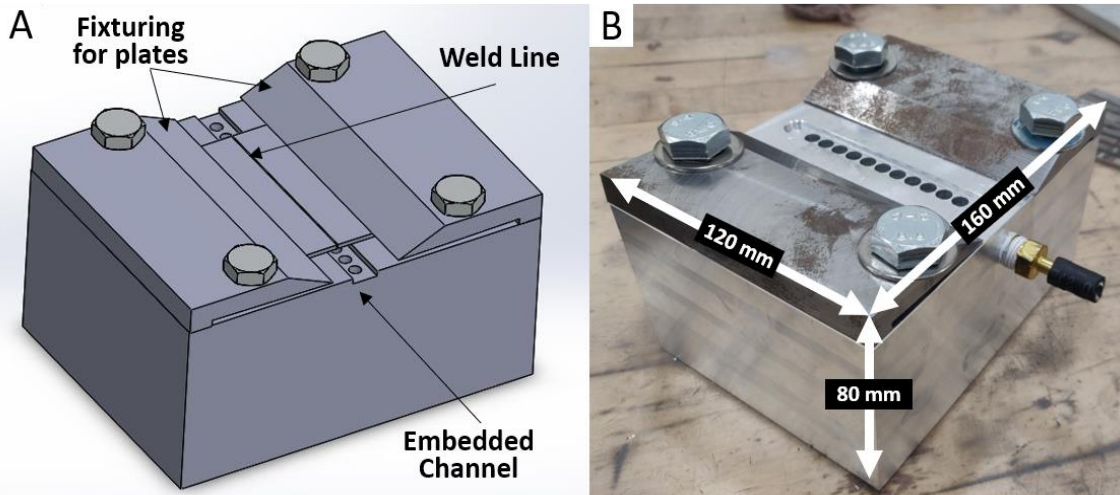
Supplementary Figure 5:A) 3D CAD model Assembly and B) Welding Setup

Supplementary Figure 4: Final specimen design

34

Supplementary Figure 6: Specimen failure of location under uniaxial tensile testing: A) W-W non-corroded broke at weld B) W-3D non-corroded broke at wrought side C) W-3D non-corroded broke at weld D) W-3D corroded broke at weld

Supplementary Figure 7 Equivalent circuit used for fitting Nyquist plot for Electrochemical Impedance Spectroscopy (EIS) test